The Astrophysical Journal, 891:56 (13pp), 2020 March 1 https://doi.org/10.3847/1538-4357/ab744b

Response of Pickup Ions in the Very Local Interstellar Medium to Solar Variations: Implications for the Evolution of the *IBEX* Ribbon and Interstellar Helium

E. J. Zirnstein[1], T. K. Kim[2], P. Mostafavi[1,3], J. Heerikhuisen[4,5], D. J. McComas[1], and N. V. Pogorelov[2,5]
[1] Department of Astrophysical Sciences, Princeton University, Princeton, NJ 08544, USA; ejz@princeton.edu
[2] Center for Space Plasma and Aeronomic Research, University of Alabama in Huntsville, Huntsville, AL 35805, USA
[3] Johns Hopkins University Applied Physics Laboratory, Laurel, MD 20723, USA
[4] Department of Mathematics and Statistics, University of Waikato, Hamilton, New Zealand
[5] Department of Space Science, University of Alabama in Huntsville, Huntsville, AL 35899, USA
Received 2019 November 19; revised 2020 January 28; accepted 2020 February 6; published 2020 March 4

Abstract

The *Interstellar Boundary Explorer* (*IBEX*) observes the "ribbon" of enhanced energetic neutral atom (ENA) fluxes from the outer heliosphere. The ribbon flux is likely formed from the neutralization of energetic pickup ions (PUIs) gyrating in the interstellar magnetic field outside the heliopause. *Voyager 1* crossed the heliopause in 2012 and has observed several shocks in the very local interstellar medium (VLISM) that likely originate from merged interaction regions in the inner heliosphere that propagated outside the heliopause. We simulate the response of PUIs and the *IBEX* ribbon flux to solar disturbances propagating into the VLISM. First, we show that PUIs outside the heliopause respond significantly to the dynamic neutralized solar wind (SW) via charge exchange and to interactions with shocks via adiabatic heating/cooling. However, the evolution of ribbon fluxes at 1 au is primarily driven by changes in the neutralized SW and not PUI interactions with shocks outside the heliopause. Comparisons with *IBEX* observations of the ribbon at 1.1 keV show that an abrupt decrease in ENA fluxes observed in 2012 was caused by a drop in SW (and thus neutralized SW) speed by $\sim$100 km s^{-1}. Our simulation predicts a recovery of 1.1 keV ribbon fluxes starting in 2019 to levels observed early in the mission owing to an increase in SW speed. We also estimate that the presence of interstellar helium in the VLISM reduces the effectiveness of charge-exchange sources for PUIs and reduces the model ribbon flux at 1 au by $\sim$40%, matching well with *IBEX* ribbon fluxes.

Unified Astronomy Thesaurus concepts: Heliosphere (711); Solar wind (1534); Pickup ions (1239); Interstellar medium (847); Shocks (2086); Heliosheath (710); Solar cycle (1487); Solar activity (1475)

1. Introduction

The solar wind (SW) plasma emitted from the Sun and the partially ionized gas of the local interstellar medium (LISM) interact as the Sun moves through interstellar space, forming the heliopause surrounding our solar system (e.g., Parker 1961; Baranov et al. 1979; Zank 1999). The region of influence of the SW on the LISM is typically referred to as the very local interstellar medium (VLISM; e.g., Zank 2015). While the solar and interstellar plasmas are separated at the heliopause (i.e., a tangential discontinuity), neutral atoms from the interstellar medium flow into the heliosphere and may charge-exchange with the relatively energetic SW ions. Energetic neutral atoms (ENAs) with energies ranging from $\sim$0.1 keV to tens of keV can be created from this charge-exchange process and propagate in all directions, some of which can travel toward Earth and be detected by the *Interstellar Boundary Explorer* (*IBEX*; McComas et al. 2009b). The *IBEX* spacecraft, whose prime mission is to improve our understanding of the SW–VLISM interaction at the outer heliosphere boundaries, observes neutral particles from the VLISM (e.g., McComas et al. 2009a, 2015; Möbius et al. 2009, 2015; Kubiak et al. 2014, 2016; Park et al. 2014, 2016; Bzowski et al. 2015, 2017; Leonard et al. 2015; Schwadron et al. 2015, 2016; Sokół et al. 2015; Swaczyna et al. 2015), as well as ENAs produced by charge exchange in the inner heliosheath (IHS) or outside the heliopause (e.g., McComas et al. 2009a, 2017; Dayeh et al. 2011, 2014, 2019; Funsten et al. 2013; Desai et al. 2014, 2019; Fuselier et al. 2014; Schwadron et al. 2014, 2018; Zirnstein et al. 2014, 2016a, 2017; Reisenfeld et al. 2016).

A particularly important and unexpected observation by *IBEX* in 2009 was the "ribbon," which is a nearly circular band of enhanced ENAs across the sky (McComas et al. 2009a). Following its initial observation (Funsten et al. 2009b; Fuselier et al. 2009; McComas et al. 2009a; Schwadron et al. 2009) and many subsequent models and analyses of its properties (see, e.g., McComas et al. 2014; Zirnstein et al. 2015a, 2019a and references therein), it is believed that the ribbon is very likely formed from "secondary" ENAs originating from outside the heliopause. Interstellar neutral atoms travel into the heliosphere and charge-exchange with SW protons, creating primary ENAs. While some of these ENAs can travel toward Earth and be detected by *IBEX* (depending on where they are created), others travel outside the heliopause and form a suprathermal ion component in the VLISM plasma after they experience another charge exchange. Once these suprathermal ions (at $\sim$keV energies) experience yet a third charge exchange, some can travel back into the heliosphere and be detected at Earth. The directions, $\boldsymbol{r}$, in the sky from which these secondary ENAs come are those approximately perpendicular to the local interstellar magnetic field (ISMF), $\boldsymbol{B}$, draped around the heliosphere, i.e., $\boldsymbol{B}\cdot\boldsymbol{r}=0$ (e.g., Schwadron et al. 2009; Heerikhuisen et al. 2010; Heerikhuisen & Pogorelov 2011; Zirnstein et al. 2015a). Note, however, that in reality the $\boldsymbol{B}\cdot\boldsymbol{r}=0$ surface is not planar, but curved owing to the field draping around the heliosphere, and can even have ripples caused by the solar cycle (Pogorelov et al. 2011). The asymmetric shape of the $\boldsymbol{B}\cdot\boldsymbol{r}=0$ surface is important for understanding the structure of the ribbon (Zirnstein et al. 2016b).

The majority of models and simulations of the *IBEX* ribbon have focused on studying the ribbon under steady-state SW and VLISM conditions (see, however, Frisch et al. 2010; Zirnstein et al. 2015b). Previous studies of the energetic PUI component (which we refer to as "pickup ions from neutral solar wind," or PINS) outside the heliopause aim to understand the stability, or lack thereof, of the PINS distribution (e.g., Florinski et al. 2010, 2016; Liu et al. 2012; Summerlin et al. 2014; Niemiec et al. 2016; Min & Liu 2018; Roytershteyn et al. 2019) and its resulting effects on the properties of the ribbon (e.g., Chalov et al. 2010; Gamayunov et al. 2010, 2017, 2019; Heerikhuisen et al. 2010; Möbius et al. 2013; Schwadron & McComas 2013; Isenberg 2014, 2015; Zirnstein et al. 2018a, 2019a). In this study, we shift the focus to how the PINS respond to solar disturbances that propagate outside the heliopause. A recent study showed that shocks propagating through the outer heliosphere can significantly increase the production rate of ENAs from the IHS, yielding a better match to *IBEX* observations than what has previously been published (Mostafavi et al. 2019). Shocks have also been observed outside the heliopause by *Voyager 1* (e.g., Burlaga et al. 2013; Gurnett et al. 2013, 2015; Rankin et al. 2019). The behavior of PINS in the presence of shocks that travel from the Sun through the VLISM is the focus of this study.

In the following sections, we first describe the 3D time-dependent simulation of the SW–VLISM interaction we use to simulate the heliosphere and propagation of solar disturbances through the VLISM (Section 2.1). Then, we describe the PINS distribution model that is used to produce the PINS distribution outside the heliopause, as well as the Parker transport equation that solves the evolution of the PINS distribution in energy, space, and time (Section 2.2). Finally, we present the results of the model, the behavior of PINS due to shocks and the time-dependent neutralized SW, and the evolution of the ribbon's source and ENA fluxes observed at 1 au over time (Section 3). A final discussion and summary of the main results of the study are provided in Section 4.

2. Model

2.1. Global Heliosphere Simulation

To simulate the propagation of SW structures and the neutralized SW outside the heliopause, we utilize the results of a 3D time-dependent, magnetohydrodynamic (MHD) simulation of the heliosphere within the framework of the Multi-scale Fluid-Kinetic Simulation Suite (MS-FLUKSS; Pogorelov et al. 2014 and references therein). The particular simulation that we use was performed by Kim et al. (2016, 2017) to successfully re-create the propagation of solar disturbances such as interplanetary coronal mass ejections and globally merged interaction regions that were observed by *Voyager 1* outside the heliopause (Burlaga et al. 2013). The simulation solves the MHD equations for a single-fluid plasma (consisting of the SW ion and PUI mixture) and four separate Euler equations for the multifluid neutral population, where the plasma and neutrals are coupled by charge-exchange source terms (e.g., Zank et al. 1996; Pogorelov et al. 2006).

The simulation is solved on a spherical grid with resolution based on adaptive mesh refinement, which allows us to resolve shocks at large distances from the Sun, especially near the heliopause and outside the VLISM. For the purposes of this study, we fix the resolution in time at a sufficiently high resolution in order to resolve shocks outside the heliopause where PINS are created. The resolution in the radial direction $\Delta r = 0.07$, 0.09, 0.1, and 0.18 au at $r = 80$, 100, 120, and 140 au, respectively. In the transverse directions, the angular resolution is approximately $0.^{\circ}7$ between radial distances $r = 65$ and 250 au and $2.^{\circ}8$ elsewhere.

The inner boundary conditions of the simulation start at 1 au, which are derived from OMNI daily averaged observations of the SW at low latitudes and *Ulysses* observations fit by empirical functions to emulate the polar coronal holes at high latitudes (see Figure 1 in Kim et al. 2017). The SW boundary conditions at low latitudes are updated at every time step by filling the 360° longitude centered on the current time's meridian with the surrounding ±13 days of OMNI data interpolated onto the simulation grid. The simulation is performed in two steps for computational efficiency. First, the SW is propagated from 1 to 12 au with a base grid size of $256 \times 128 \times 64$ cells. Then, at 12 au the grid size of the simulation is changed to $640 \times 128 \times 64$ cells to simulate the SW–VLISM interaction.

The outer boundary conditions of the VLISM at 1000 au are constrained by *IBEX* observations, where the inflow speed is 25.4 km s^{-1}, the inflow direction in ecliptic J2000 is ($255.^{\circ}7$, $5.^{\circ}1$), the plasma/neutral temperature is 7500 K (McComas et al. 2015), and the total effective plasma and neutral H densities are 0.09 and 0.154 cm^{-3}, respectively, which are found by Zirnstein et al. (2016b) to produce a neutral H density at the termination shock (TS) in the noseward direction of ~0.1 cm^{-3}, consistent with a consolidation of different modeling and data analysis techniques (Bzowski et al. 2009). The ISMF magnitude (3 μG) and direction ($226.^{\circ}99$, $34.^{\circ}82$) are based on the best model fit by Zirnstein et al. (2016b) to the position of the *IBEX* ribbon (see Table 1 in Zirnstein et al. 2016b). For more details of the heliosphere simulation, see Kim et al. (2016, 2017).

We note that it is important to track the location of the heliopause in this study since it moves inward and outward over time owing to changes in the SW properties. In our simulation, the heliopause is defined as a critical stream surface, where both the SW and VLISM plasma velocity vectors are parallel to the surface and have no normal component. We use the level set method (Sethian 1999; Osher & Fedkiw 2002) implemented in MS-FLUKSS by Borovikov et al. (2011) during the heliosphere simulation to track the surface separating the SW and VLISM plasmas (i.e., heliopause).

2.2. Pickup Ion Transport Equation

We solve the time-dependent Parker transport equation (e.g., Parker 1965) with charge-exchange source terms assuming that PINS are advected with the bulk plasma, PINS experience adiabatic acceleration, and the production and loss of PINS are governed by charge-exchange interactions with neutral H. The transport equation is given by

$$\frac{\partial f}{\partial t} + u_{\mathrm{p,r}}\frac{\partial f}{\partial r} = \frac{v}{3}(\nabla \cdot \boldsymbol{u}_{\mathrm{p}})\frac{\partial f}{\partial v} + P - L, \tag{1}$$

where $f(r, t, v)$ is the PINS distribution, $u_{\mathrm{p,r}}(r, t)$ is the bulk plasma speed from the MHD simulation projected onto the radial direction ($\boldsymbol{u}_{\mathrm{p}} \cdot \hat{\boldsymbol{r}}$), v is the particle speed, $\nabla \cdot \boldsymbol{u}_{\mathrm{p}}$ is the

flow divergence, and $P(r, t, v)$ and $L(r, t, v)$ are the production and loss source terms, respectively, of PINS from charge exchange with neutral H. The methods for solving Equation (1) are explained in more detail in the Appendix.

We assume that PINS outside the heliopause interact adiabatically with shocks propagating outside the heliopause. We make this assumption based on recent work by Mostafavi & Zank (2018a, 2018b), who showed that PINS outside the heliopause behave nearly adiabatically at shocks and do not significantly mediate the shock interaction (i.e., via collisions or wave–particle interactions). Rather, proton–proton collisions of the thermal ion component of the interstellar plasma determine the shock thickness and dominate the energy dissipation. With this assumption, the flow divergence term in Equation (1) is used to model the interaction of the particle distribution with shocks and compressions propagating outside the heliopause. We note, however, that while PINS may behave adiabatically at the shock interaction, the production of PINS in the VLISM by charge exchange effectively modifies the shock's properties by changing the upstream plasma conditions, in particular the heliospheric boundary layer outside the heliopause that is modified by charge exchange (e.g., Pogorelov et al. 2017). In this way, PINS may experience nonadiabatic behavior upstream or downstream of the shock due to charge exchange.

We solve Equation (1) in one spatial dimension (i.e., the radial direction) using plasma and neutral properties from a 3D simulation of the heliosphere–VLISM interaction. This assumption means that PINS are advected along the radial direction with the radial component of the bulk plasma flow. The radial lines of sight that we simulate are within 30° of the pristine interstellar flow direction, and therefore the assumption of radial advection is approximately accurate at large distances from the heliopause (i.e., tens of astronomical unit). However, near the heliopause, the interstellar plasma is slowed and diverted away from the radial direction. A fraction of the ribbon flux is created within this region of space. Nevertheless, we argue that this is a reasonable assumption for our purposes since the advection time for PINS outside the heliopause is large compared to the charge exchange and adiabatic heating timescales. For example, the flow speed is $<20\,\mathrm{km\,s^{-1}}$ in the PINS production region (within ∼100 au of the heliopause). With a $1/e$ charge-exchange time of 2.5 yr for a 1.1 keV proton, the PINS will advect <10 au, which is much smaller than the heliospheric interaction region. The adiabatic heating rate for PINS in the vicinity of shocks, as we show later in Section 3.3, is typically $>10^{-7}\,\mathrm{s^{-1}}$, which corresponds to a timescale <0.3 yr. The PINS production rate is smaller than the adiabatic heating rate in the vicinity of shocks in most cases based on our modeling results (see Section 3.3). Moreover, we have tested the effects of this assumption on our results by neglecting the advection term in Equation (1) at various times during the simulation. The resulting ENA fluxes at 1 au do not change significantly since the advection term is small compared to the other terms.

The adiabatic heating term is solved using the continuity equation,

$$\frac{\partial \rho_{\rm p}}{\partial t} + \nabla \cdot (\rho_{\rm p} \boldsymbol{u}_{\rm p}) = 0, \tag{2}$$

where $\rho_{\rm p}$ is the mass density of the bulk plasma. Using Equation (2), the divergence of the flow is written as

$$\nabla \cdot \boldsymbol{u}_{\rm p} = -\left(\frac{\partial \ln \rho_{\rm p}}{\partial t} + u_{\rm p,r} \frac{\partial \ln \rho_{\rm p}}{\partial r} \right). \tag{3}$$

For the charge-exchange production (P) and loss (L) terms, we utilize the multifluid neutral populations from the MHD simulation as source terms. The fluid approximation allows us to simplify the source terms as

$$\begin{aligned} P(r, t, v) &= f^*(r, t, v) n_{\rm p}(r, t) \sigma_{\rm ex}(v) v, \\ L(r, t, v) &= f(r, t, v) n_{\rm H}(r, t) \sigma_{\rm ex}(v) v, \end{aligned} \tag{4}$$

where $\sigma_{\rm ex}(v)$ is the energy-dependent, charge-exchange cross section (Lindsay & Stebbings 2005) and $f^*(r, t, v)$ is the PINS distribution injected by the ionization of the neutralized SW distribution.

We note that the derivation of Equation (4) assumes that (1) the interstellar plasma and neutral distributions are Maxwell-Boltzmann and (2) the relative speed of interaction between the plasma and neutral populations is dominated by the speed of the PINS particle. The latter is a reasonable assumption since the bulk flow and thermal speeds of the interstellar plasma and neutral populations are $\sim 20\,\mathrm{km\,s^{-1}}$, which is much less than the speed of a 1.1 keV proton ($460\,\mathrm{km\,s^{-1}}$). Swaczyna et al. (2019) found that it is possible that the interstellar plasma may be kappa-like, best represented with a kappa distribution with kappa index >3.8 but with higher temperature than previously thought. While a kappa index >3.8 is not exactly in equilibrium, it is approximately near equilibrium (e.g., Livadiotis & McComas 2011) such that we can assume for our model that the interstellar plasma and neutral populations are Maxwellian for the purposes of simplifying Equation (4).

2.3. Pickup Ion Production Source Term

The PINS distribution, f^*, injected by the ionization of the neutralized SW distribution (note that we only include neutral atoms from the supersonic SW, although other ∼keV neutral atoms are present but in lower numbers; Heerikhuisen et al. 2016) is determined from the "weak scattering" theory (e.g., Chalov et al. 2010; Zirnstein et al. 2018a, 2019b). Similar to Zirnstein et al. (2019b), we integrate over the gyrophase of PINS (Ω) with a small spread in pitch angle, $\Delta\varphi$, yielding

$$f^*(r, t, v) = \frac{1}{\Delta\varphi} \int_{-\Delta\varphi/2}^{+\Delta\varphi/2} \times \left(\frac{1}{2\pi} \int_0^{2\pi} S_{\rm NSW}(r, t, v, \Omega, \varphi) d\Omega \right) d\varphi. \tag{5}$$

We set $\Delta\varphi = 5°$, which produces a relatively narrow PINS ring beam. The stability and thus pitch-angle width over time of PINS ring beams outside the heliopause are a subject of debate. However, it has been proposed by Florinski et al. (2016) that a narrow ring beam that is, initially, slightly broadened in pitch angle may remain stable over a long period of time in the presence of a warm background plasma. Based on the simulation results of Florinski et al. (2016), we decide to fix $\Delta\varphi = 5°$ in this study. However, we note that we have tested the results of our model by setting $\Delta\varphi = 2°$ and 10°. While there are small differences in ENA fluxes over time, on average

the results are robust. In fact, the standard deviation of model ENA fluxes between the cases for $\Delta\varphi = 2°$, 5°, and 10° over the 2009–2018 epoch is <10%. Thus, our results do not significantly depend on our choice of $\Delta\varphi$, under the assumption that the PINS distribution must still be a relatively narrow ring beam.

The neutralized SW source term, $S_{\rm NSW}$, is given by

$$S_{\rm NSW}(r,\,t,\,v,\,\Omega,\,\varphi) = \frac{n_{\rm NSW}(r,\,t)}{\pi^{3/2}\delta v_{\rm r}\delta v_{\rm tr}^2} \times \exp\left(-\left(\frac{v_{\rm r}-u_{\rm NSW,r}(r,\,t)}{\delta v_{\rm r}}\right)^2 - \left(\frac{v_{\rm tr}(v,\,\Omega,\,\varphi)}{\delta v_{\rm tr}(r)}\right)^2\right), \quad (6)$$

where we assume that the neutralized SW distribution is bi-Maxwellian in the radial and transverse directions. Note that while the multifluid simulation does provide the density ($n_{\rm NSW}$) and radial bulk speed ($u_{\rm NSW,r}$) of the neutralized SW, it does not distinguish these radial and transverse components; therefore, we estimate the radial and transverse spreads of the distribution as described below. We generate a PINS distribution that can be observed by *IBEX*, whose line of sight is approximately along the radial direction. Thus, we determine the radial and transverse components of PINS created from the neutralized SW distribution as

$$v_{\rm r}(v,\,\Omega,\,\varphi) = \boldsymbol{v}(\Omega,\,\varphi)\cdot\hat{\boldsymbol{r}},$$
$$v_{\rm tr}(v,\,\Omega,\,\varphi) = v\sin\left(\cos^{-1}(\hat{\boldsymbol{v}}(\Omega,\,\varphi)\cdot\hat{\boldsymbol{r}})\right), \quad (7)$$

where $v_{\rm r}$ is the PINS speed projected in the radial direction and $v_{\rm tr}$ is the projection in the transverse direction. The thermal spread in the transverse direction is given by

$$\delta v_{\rm tr}(r) = \sqrt{\frac{2k_{\rm B}T_{\rm tr,TS}}{m_{\rm p}}\left(\frac{r_{\rm TS}}{r}\right)^2}, \quad (8)$$

where $r_{\rm TS}$ is the radial distance from the Sun to the TS. We estimate the transverse temperature of the neutralized SW distribution at the TS, $T_{\rm tr,TS}$, to be 5000 K, which then decreases with distance as r^{-2} (Florinski & Heerikhuisen 2017). The thermal spread of the neutralized SW in the radial direction is calculated from the multifluid simulation using the temperature of the neutral fluid, $T_{\rm NSW}$. The single-fluid temperature is a combination of radial and transverse components; therefore, we estimate the radial thermal spread, $\delta v_{\rm r}$, as

$$\delta v_{\rm r}(r,\,t) = \sqrt{3\left(\frac{2k_{\rm B}T_{\rm NSW}(r,\,t)}{m_{\rm p}}\right) - 2\delta v_{\rm tr}^2(r)}, \quad (9)$$

under the assumption that the total thermal spread of the neutral SW distribution from the multifluid simulation is given by $\delta v_{\rm NSW}^2 = \delta v_{\rm r}^2/3 + 2\delta v_{\rm tr}^2/3$. We assume that $\delta v_{\rm tr}$ does not change with time in our model since we do not have sufficient knowledge from the simulation to determine their time dependence. We note that our choice of setting $T_{\rm tr,TS} = 5000$ K is based on a steady-state calculation of the time-averaged SW, assuming an SW speed of 450 km s^{-1} and temperature of 100,000 K at 1 au (see Florinski & Heerikhuisen 2017). In reality, the SW speed and temperature change over time. While variations in SW properties are taken into account in the MHD simulation, our assumption of constant $T_{\rm tr,TS}$ means that our ribbon model does not account for changes in neutral SW transverse temperature. It has been observed that the SW proton temperature increases with SW speed, up to a few hundred thousand kelvin (e.g., Elliott et al. 2016). To first order, this suggests that the transverse temperature for the neutral SW may sometimes be larger by a factor of ∼2–3 for faster SW. It is not exactly clear how $T_{\rm tr,TS}$ of the neutral SW at larger distances from the Sun should change over time; thus, we assume that $T_{\rm tr,TS}$ is constant. Consequences for our modeling assumption are discussed in more detail in Section 4.1. However, we note that $\delta v_{\rm tr}$ is small compared to $\delta v_{\rm r}$ (e.g., ∼5 km s^{-1} vs. ∼100 km s^{-1}), and therefore we expect that changes in $\delta v_{\rm tr}$ should not significantly affect the main results of this study.

The main results of this study presented in Section 3 do not qualitatively depend on the specific ribbon model that we employ. We note that we have tested the results using the "spatial retention" model from Schwadron & McComas (2013) as simulated by Zirnstein et al. (2019a); however, the simulated ENA intensity is significantly smaller than that observed by *IBEX* when implemented in our model. This is likely due to differences in the interstellar plasma and neutral densities outside the heliopause from our MHD simulation and those assumed by Schwadron & McComas (2013). It is also important to note that the presence of interstellar He may require reconsideration of our assumptions for the VLISM H^+ and H densities and thus may change the effective charge-exchange rates outside the heliosphere. This is discussed in more detail in Section 4.2.

2.4. ENA Flux at 1 au

We compute the time-dependent ENA flux at 1 au following our previous work (e.g., Zirnstein et al. 2015b), i.e., the flux of ENAs produced in the outer heliosphere that propagate to 1 au and are observed by *IBEX*. The differential ENA flux ($J_{\rm ENA}$) is given by

$$J_{\rm ENA}(t,\,v) = \int_E\left[\int_r \frac{1}{m_{\rm p}}f(r,\,t,\,v_{\rm p})vS(r,\,t,\,v)n_{\rm H}(r,\,t)\, v_{\rm rel}(|\boldsymbol{v}-\boldsymbol{u}_{\rm H}|)\sigma_{\rm ex}(v_{\rm rel})dr\right] \times W_{\rm ESA}(E)dE, \quad (10)$$

where $m_{\rm p}$ is the proton mass, f is the local PINS distribution, $v_{\rm p} = |\boldsymbol{v}-\boldsymbol{u}_{\rm p}|$ is the ENA speed in the plasma frame, S is the ENA survival probability from ionization, and $v_{\rm rel}$ is the relative speed of interaction between the proton and neutral H distribution. The local time t at some distance r from the Sun is calculated as $t = t_{\rm m} - r/v$, where $t_{\rm m}$ is the ENA measurement time and v is the ENA speed. Equation (10) is integrated along the radial direction as a function of time from 1 to 200 au from the Sun (which includes the majority of ENA production; see Section 3.1).

Similar to Equation (4), we reasonably assume that $v_{\rm rel} \cong v$. The ENA survival probability is calculated from the point of ENA creation to 100 au from the Sun. ENAs do experience losses all the way to 1 au before detection; however, *IBEX* observations are corrected for ENA survival probability from 1 to 100 au using time-dependent OMNI data at 1 au

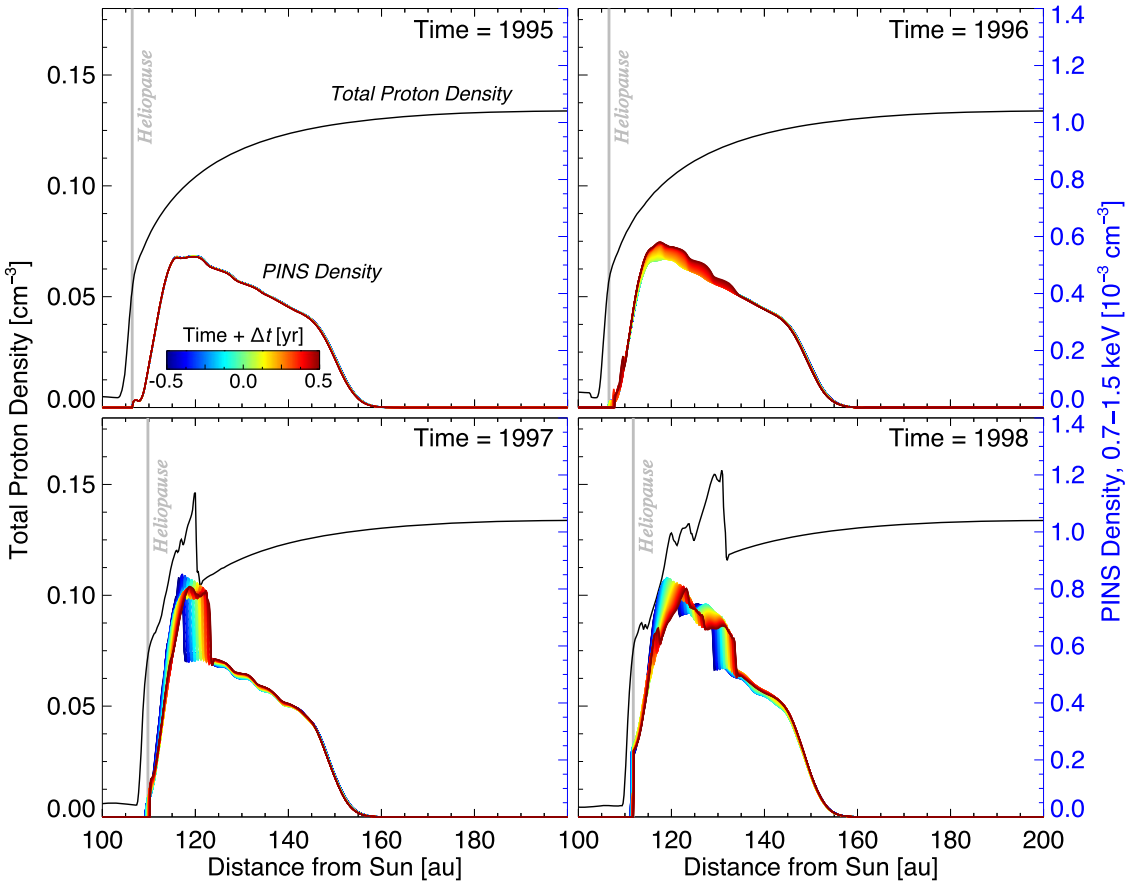

Figure 1. Total proton density (black) and PINS density (red to blue spectrum) from 0.7 to 1.5 keV outside the heliopause toward ecliptic J2000 (278°, −9°). The location of the heliopause is denoted by the vertical gray line. In the top left panel (time = 1995), the initial steady-state conditions are shown. We only show the total proton density at exactly the time listed in the upper right of each panel. We show the PINS density at a range of times ±0.5 yr from the time shown in the upper right of each panel, where the time range is shown as the color spectra.

(e.g., McComas et al. 2017). The correction for the ENA survival probability is likely more accurate than our simulation of ENA losses; thus, we compare with the survival probability-corrected *IBEX* data. For accurate comparisons with *IBEX* observations, Equation (10) is integrated over the *IBEX-Hi* energy response function, $W_{\rm ESA}$, for the particular electrostatic analyzer (ESA) energy step (Funsten et al. 2009a).

3. Results

In this section we present results from modeling the spatial and temporal properties of the PINS distribution outside the heliopause. Their distribution is affected not only by shocks propagating away from the heliopause but also by the time-dependent neutralized SW distribution that affects the rate of PINS injection by charge exchange. Comparisons of these two effects on the PINS distribution and on ENA fluxes at 1 au are discussed below.

3.1. Initial Reaction of PUIs and ENAs to a Strong Shock outside the Heliopause

The global heliosphere simulation is initially run to produce a steady state of the SW–VLISM interaction before time-dependent boundary conditions are introduced (time-dependent boundary conditions begin in 1995). In Figure 1 we show the steady-state distribution (in 1995) of total proton density (from the MHD simulation) and the steady-state PINS density integrated from 0.7 to 1.5 keV. Initially, the total proton density increases smoothly as a function of distance from the heliopause to a value of $\sim$0.125 cm^{-3} near 150 au from the Sun and decreases to 0.09 cm^{-3} ahead of the bow wave (not shown). The PINS density maximizes close to the heliopause (heliopause at $\sim$105 au, PINS density maximum at $\sim$120 au), where the ISMF is draped such that PINS, once converted to ENAs, would be preferentially observed at 1 au by *IBEX* (i.e., where $\boldsymbol{B}\cdot\boldsymbol{r}=0$).

After 1995, solar disturbances injected into the simulation using observations from the OMNI database at 1 au have reached the outer heliosphere and propagated outside the heliopause. The dynamic SW conditions are preceded by a strong shock that propagates outside the heliopause starting after 1996. Both the total proton density and the PINS distribution increase significantly ($\sim$30%–50%) as the shock propagates away from the heliopause. The shock is traveling approximately 10 au yr^{-1}, or 50 km s^{-1}, this close to the heliopause. Note, however, that before the shock propagates outside the heliopause, the PINS density already starts increasing owing to an increase in PINS production by charge exchange from neutral SW atoms.

Before we continue, we look at the reaction of ENA fluxes at 1 au to the strong shock shown in Figure 1. As the dynamic SW conditions are advected to the outer heliosphere and away from the heliopause, the fluxes of ENAs at 1 au will likely increase owing to the enhancement in plasma density and the ENA production rate. The time over which ENAs at 1 au will react

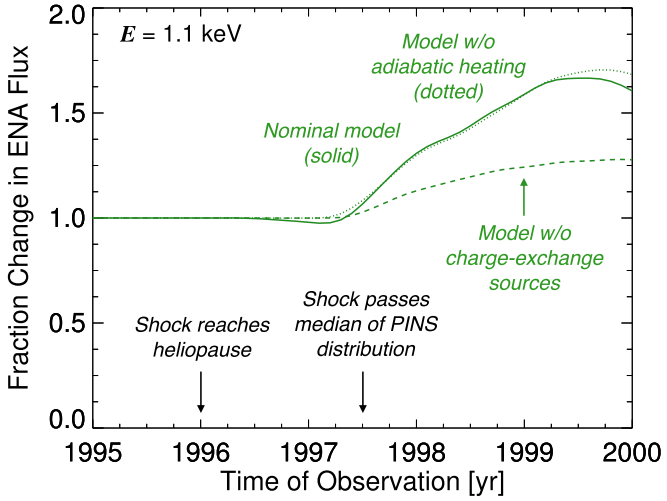

Figure 2. Simulated ENA fluxes at 1 au after the start of the heliosphere simulation (initial time = 1995), normalized to the initial flux value. The direction in the sky is (278°, −9°) in ecliptic J2000. The heliosphere simulation is initially in steady state before dynamic SW conditions preceded by a strong shock are introduced into the simulation at 1995. A response to the strong shock is initially seen in ENA fluxes at 1 au in late 1997. Note that for the models without adiabatic heating (dotted, $\nabla \cdot \boldsymbol{u}_{\rm p} = 0$) and charge-exchange source terms (dashed, $P - L = 0$) we also set $u_{\rm p} = 0$ to remove transport effects.

depends on the charge-exchange rate and distance from their source to 1 au. Figure 2 shows the (normalized) evolution of ENA fluxes in response to changes in the simulation. The dynamic SW conditions were introduced into the simulation at 1 au in 1995.0, and it took ∼1 yr for them to reach the heliopause and another ∼1.5 yr for the initial shock to propagate halfway through the PINS production region (see Figure 1, bottom left panel—in mid-1997, the shock has propagated to 125 au, which is the "median" of the PINS source distribution). ENA fluxes at 1 au are beginning to respond in mid-1997, and by mid-1999 they have reached a local maximum increase of ∼60%.

The time it takes 1.1 keV ENAs to travel over a distance of 120 au is ∼1.2 yr. This implies that as soon as the shock reached the PINS source distribution in mid-1996, we begin to see changes in ENAs approximately 1 yr later at 1 au. ENA fluxes at 1 au increase at a relatively slow rate compared to the shock jump because the shock must move through the majority of the PINS source distribution before the ENA production rate maximizes at 1 au 1 yr later. It takes about 1.5 yr for the shock to propagate from the heliopause to the median of the PINS source distribution, and another 2 yr for the ENA fluxes to reach a local maximum at 1 au.

We point out that the reaction time of ENA fluxes at 1 au that originate outside the heliopause to this shock is significantly quicker than what one might expect with a delay owing to the "$1/e$" charge-exchange time, $\tau_{\rm ex} = 1/(n_{\rm H}\sigma_{\rm ex}v)$. The charge-exchange lifetime has an exponential drop-off over time, such that the average lifetime of a particle is heavily weighted by the long lives of a small fraction of particles. Usually, it is expected that the time for ENAs from outside the heliopause to respond to changes in the SW is an accumulation of (1) the time it takes changes in the SW to propagate outside the heliopause to the ENA source region, (2) the time it takes for a significant number of PINS to experience charge exchange and become secondary ENAs, and (3) the time it takes for the secondary ENAs to travel back to 1 au. Considering that the SW takes 2.5 yr to travel to the median of the PINS source distribution, the ENA travel time back to 1 au is approximately 1.2 yr, and the $1/e$ charge-exchange lifetime for a 1.1 keV PINS outside the heliopause is 2.7 yr (for neutral H density of 0.15 $\rm cm^{-3}$), the total accumulated delay time is expected to be ∼6.4 yr. However, as we have shown in Figures 1 and 2, the time it takes to first see a significant (∼10%) change in ENAs is 2.5 yr, the majority of which is just the time for propagation to and from the edge of the PINS source distribution. Thus, large enough changes in the SW may first be observed in directions of the ribbon in as little time as it takes to propagate there and back. It is commonly assumed that the average response time of ENAs observed at 1 au to changes in the SW is due not only to the time for propagation to the OHS and back toward 1 au but also to the $1/e$ charge-exchange production timescale, typically calculated as $1/(n_{\rm p}\sigma_{\rm ex}v) \sim$ 2–3 yr for 1 keV particles. However, this timescale represents the time over which 63% of particles have already experienced charge exchange. Thus, our results predict that we should see changes in ENA fluxes at 1 au sooner than the average charge-exchange delay time.

3.2. Evolution of PUIs outside the Heliopause

Figure 3 shows the evolution of the total proton and PINS densities over time as these structures propagate through the OHS. First, it is clear that the PINS source region moves away from the heliopause over time as the shocks propagate through the OHS. This is due to a change in the draping of the ISMF around the heliosphere. The location where the PINS distribution (observable as ENAs at 1 au) maximizes is where $\boldsymbol{B} \cdot \boldsymbol{r} \sim 0$. Thus, it is interesting to note that in a steady-state simulation of the heliosphere, the ribbon source location is closer to the heliopause by a few tens of au than in a time-dependent simulation owing to fluctuations in the draping of the ISMF around the heliosphere (at least, in this direction of the sky; e.g., Pogorelov et al. 2011).

The effects of shocks on the PINS distribution in the OHS are also visible in Figure 3. PINS are adiabatically heated whenever a shock propagates past, creating enhancements in their energy density. These can be seen as small "ripples" in the PINS density. While interstellar shocks affect the PINS distribution outside the heliopause, in Section 3.5 we show how much they determine the evolution in ribbon ENA fluxes observed at 1 au.

3.3. Adiabatic Heating versus Charge Exchange

In this section we quantify how important adiabatic heating is compared to charge exchange in the vicinity of shocks. In order to make a direct comparison of these rates, we compute them as follows:

$$R_{\rm ad}|_{i,j}^{k} = -\frac{(\nabla \cdot \boldsymbol{u}_{{\rm p},i}^{k-1})}{3}\frac{\partial f}{\partial w}\Bigg|_{i,j}^{k-1}\frac{1}{f_{i,j}^{k-1}},$$

$$R_{\rm ex}|_{i,j}^{k} = (P_{i,j}^{k-1} - L_{i,j}^{k-1})\frac{1}{f_{i,j}^{k-1}} = \left(\frac{f_{i,j}^{*k-1}}{f_{i,j}^{k-1}}n_{{\rm p},i}^{k-1} - n_{{\rm H},i}^{k-1}\right)\sigma_{\rm ex}v, \quad (11)$$

where $R_{\rm ad}$ and $R_{\rm ex}$ are the adiabatic heating and charge-exchange rates at time step k, respectively. We normalize the rates by the PINS distribution at time step $k-1$ ($f_{i,j}^{k-1}$) in order

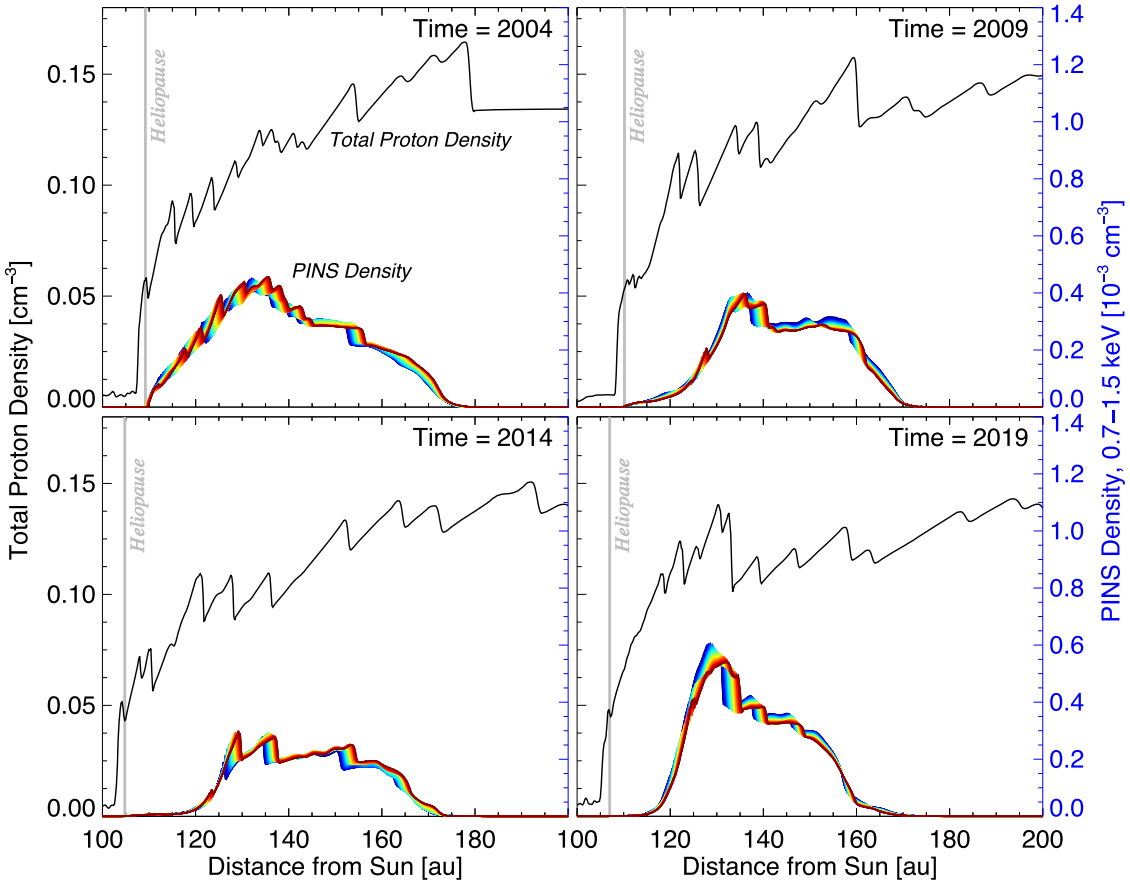

Figure 3. Similar to Figure 1, but at later times. The time range of PINS density is shown as color spectra, similar to Figure 1.

to quantify the effectiveness of the process on changing the distribution. Figure 4 shows a comparison of these rates at 140 au from the Sun, which is approximately in the center of the PINS distribution in 2015–2019.

As can be seen in Figure 4, during the passage of shocks across the PINS distribution, the rate of adiabatic heating process dominates over charge exchange. In this example, the rate of adiabatic heating is approximately an order of magnitude larger than the charge-exchange source term. Therefore, adiabatic heating is primarily responsible for accelerating particles in the vicinity of shocks compared to enhancements in the production rate of PINS. However, as we show in Section 3.5, the neutral SW is primarily responsible for the evolution of the ENA fluxes at 1 au.

3.4. Evolution of ENA Fluxes at 1 au

After simulating the PINS distribution outside the heliopause, we calculate the time-dependent ENA flux at 1 au for *IBEX-Hi*'s energy passband 3, with a central energy of 1.11 keV (McComas et al. 2012). The model ENA fluxes and the observations are shown in Figure 5. We show results from modeling ENA fluxes in several different directions of the sky in ecliptic J2000 coordinates, all of which lie near the peak of the ribbon flux at low latitudes: (285°, 0°.5), (278°, −9°), and (254°, −20°). Note that in Sections 3.1 and 3.2 we only showed the PINS distribution results in direction (278°, −9°).

We compare the model to *IBEX* data collected in the ram frame of its motion around the Sun, which provides the best statistics. The data are transformed from the spacecraft to the

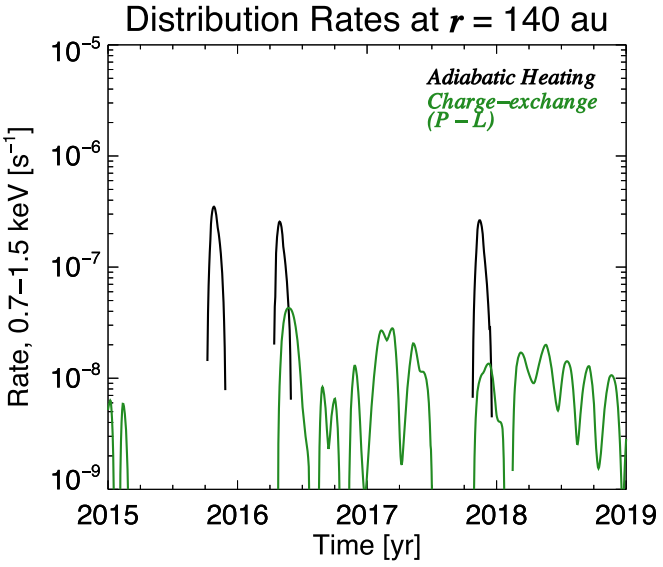

Figure 4. Comparison of adiabatic heating (black) and charge-exchange (production − loss, green) rates for the PINS distribution for energies 0.7–1.5 keV at $r = 140$ au from the Sun. The rates are calculated using Equation (11).

solar inertial frame and are corrected for the survival probability of ENAs from 100 to 1 au (thus, we do not account for ENA losses from 100 to 1 au in our model). We extract data from the 9 pixels that are nearest to each of the three directions we simulate from our model. The directions we model ENA fluxes from and the macro-pixels from which the *IBEX* data are

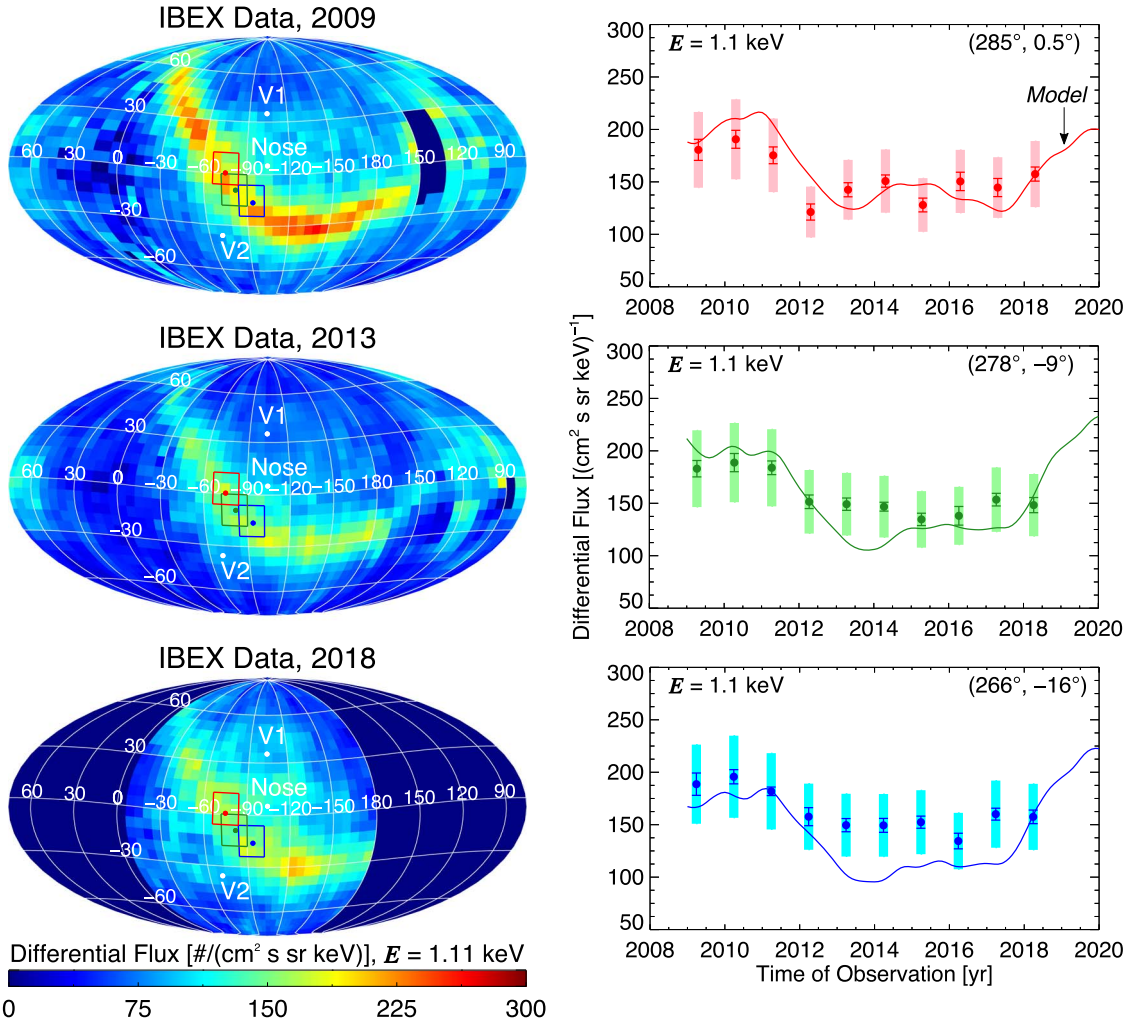

Figure 5. *IBEX* observations of ENA fluxes at 1 au (skymaps on the left, data points with uncertainties on the right) compared to simulated ENA fluxes (curves on the right). We simulate fluxes from three different directions in the sky (red, green, and blue circles in skymaps) and compare to *IBEX* data within the nearest 9 pixels (red, green, and blue boxes in skymaps). *IBEX* statistical uncertainties are shown as error bars, and the systematic uncertainties (estimated as 20% of the flux; Fuselier et al. 2014) are shown as shaded regions.

extracted are shown in Figure 5 (left panels). The weighted average of the fluxes over the 9 surrounding pixels is calculated by computing the mean of the fluxes weighted by their respective variance. The error bars shown in Figures 5, 7, and 9 are calculated from (1) the propagated uncertainty of the mean and (2) the statistical uncertainty about the mean. We also show an envelope around the data points to reflect a systematic uncertainty of 20% of the mean flux due to uncertainties in the calibration of *IBEX-Hi* (e.g., Fuselier et al. 2012, 2014). The first two uncertainties are random statistical uncertainties of the measurements and are added in quadrature to yield the final uncertainty shown in Figures 5, 7, and 9 (for more details, see Appendix C in Zirnstein et al. 2016b). Note that the systematic uncertainties dominate over statistical uncertainties.

First, both the observations and simulation results show a consistent decrease in ENA fluxes in 2012, though the model predicts a slightly larger decrease than what is observed. This decrease is strongly correlated with a decrease in the neutral SW speed from ∼475 to <400 km s^{-1} (see Figure 6). At the ENA source region (∼140 au from the Sun), this decrease in neutral SW speed starts in late 2009 and ends in late 2011. The ENA travel time from the source at 140 to 1 au is ∼1.5 yr—thus, the ENA flux at 1 au begins to decrease just after 2011. The decrease in 1.1 keV ENA fluxes is due to the difference in speed between the bulk neutral SW distribution and the speed of 1.1 keV ENAs. ENAs with energies of 1.1 keV travel at speeds of 460 km s^{-1}, which is close to the average neutral SW speed before 2010. But as the average neutral SW speed decreases after 2010, fewer 1.1 keV PINS, and thus fewer 1.1 keV ENAs, can be created. This in turn decreases the 1.1 keV ENA flux at 1 au a few years later.

The simulation predicts that the 1.1 keV ENA flux at 1 au should begin to increase after 2018 and by 2020 reach the intensity it was at before the drop in 2012. This is at least partially due to a corresponding increase in neutral SW speed (see Figure 6). The model, which utilizes in situ observations of the SW at 1 au, also shows a slow but steady increase in neutral SW density and temperature after 2014, which also contributes to an increase in ENA fluxes after 2018.

Next, we compare averages of the fluxes in all three directions shown in Figure 5. The average of the model fluxes is computed simply by calculating the mean flux over the three directions. The average of the data is computed similarly to what is described above for Figure 5 (right panels), except that the mean and their uncertainties are computed over 27 pixels instead of 9 pixels. The results are shown in Figure 7.

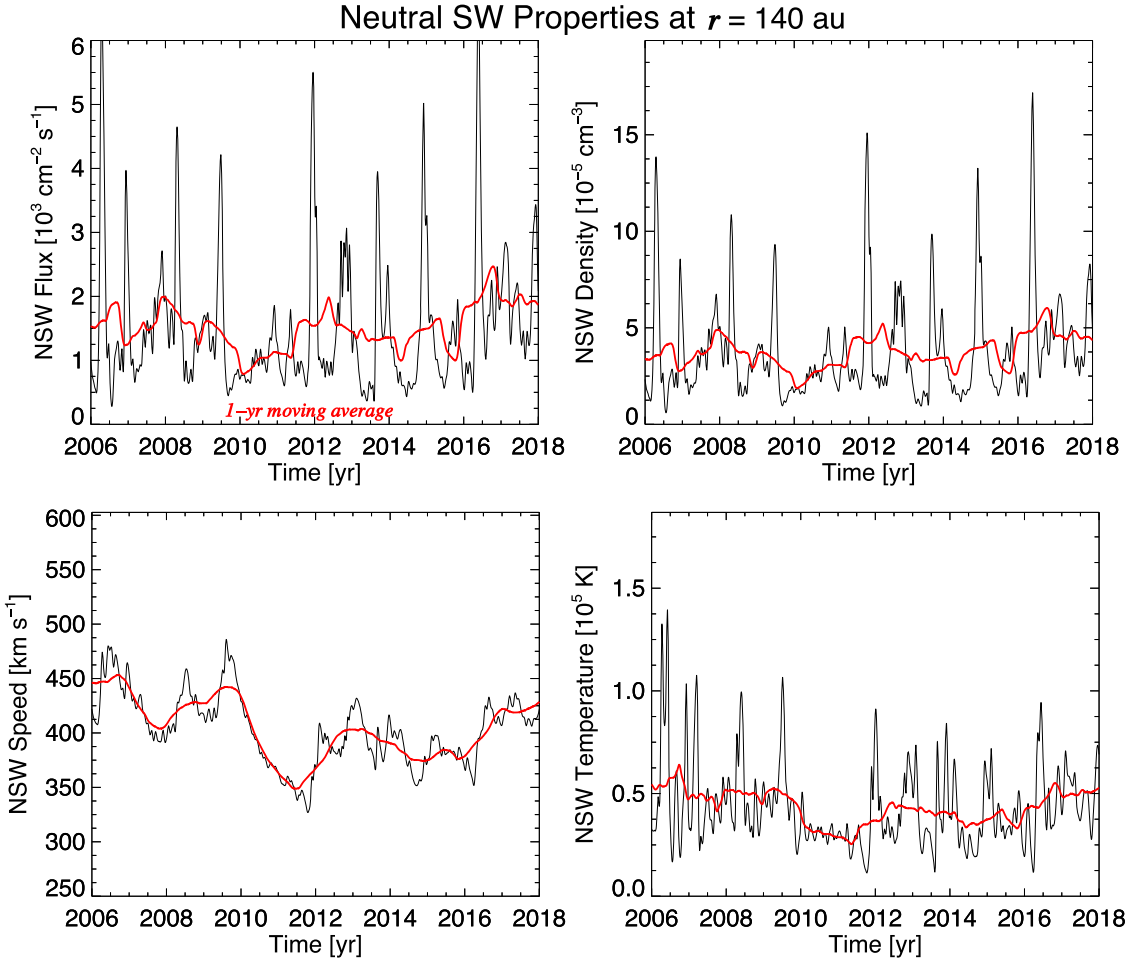

Figure 6. Neutral SW (NSW) flux, density, speed, and temperature from the multifluid heliosphere simulation as a function of time at $r = 140$ au from the Sun. The 1 yr moving averages are shown in red for each panel.

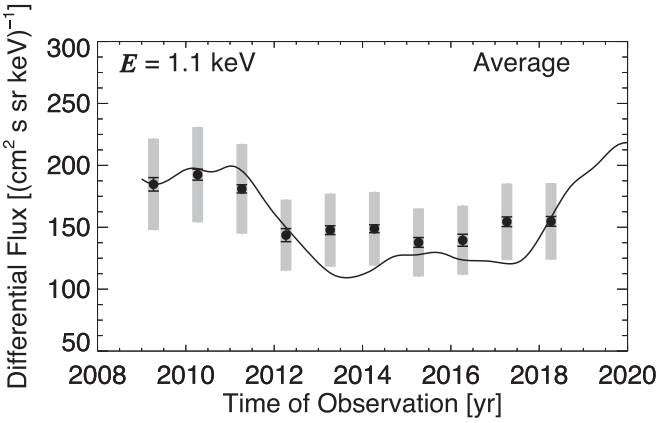

Figure 7. *IBEX* observations of ENA fluxes at 1 au (data points with uncertainties) compared to simulated ENA fluxes (curve). These are the spatial averages of the data and simulated results shown in Figure 5. Similar to Figure 5, we show *IBEX*'s statistical uncertainties (error bars) and systematic uncertainties (shaded regions).

The average simulated fluxes compare well to *IBEX* data, but the simulated fluxes in 2013, 2014, and 2017 are slightly below the observed flux. The small differences between the model and observations may be explained from several sources. First, while we are comparing to observations near the peak of the observed ribbon flux, there are still a significant number of ENAs from the globally distributed flux (GDF) originating from the IHS. Our model does not include ENA fluxes from the IHS, which may account for a few tens of percent of the total flux. However, based on the analyses by Schwadron et al. (2014, 2018), the GDF also decreases significantly after 2012. Therefore, if the observed ribbon flux and GDF both decrease in 2012, then it appears unlikely that including the GDF in the simulation results would significantly improve the comparison of our model with the observations. Second, it is likely that the simulation's approximation of the neutral SW as a fluid, which inhibits the kinetic aspect of neutral H propagation through the heliosphere, may be responsible for a discrepancy between the model and data. Third, our model does not include the presence of interstellar He, the effects of which are discussed in more detail in Section 4.2.

3.5. Are Changes in ENA Fluxes Driven by the Neutral SW or Interstellar Shocks?

We can easily test what process is primarily responsible for the evolution of ENA fluxes at 1 au: (1) the evolving neutral SW distribution, and thus its production of PINS outside the heliopause, or (2) solar disturbances propagating through the OHS that affect the production rate of PINS and adiabatic heating of the PINS distribution. Figure 8 shows ENA fluxes simulated using the nominal model (from Figure 5 in direction (278°, −9°)) and ENA fluxes simulated assuming that (1)

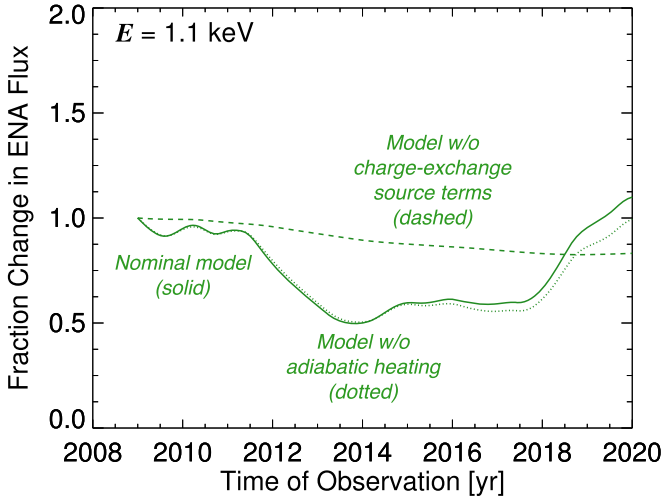

Figure 8. Simulated ENA fluxes at 1 au using three different model assumptions: (1) nominal model (solid curve), (2) a model with charge-exchange source terms turned off ($P - L = 0$) after 2005 (dashed curve), and (3) a model with adiabatic heating turned off ($\nabla \cdot \boldsymbol{u}_p = 0$) after 2005 (dotted curve). ENA fluxes are simulated from direction (278°, −9°) in ecliptic J2000 coordinates. Similar to Figure 2, we also set $u_p = 0$ to remove transport effects for the models without charge exchange and adiabatic heating after 2005.

charge-exchange source terms are turned off after 2005 and (2) adiabatic heating/cooling is turned off after 2005. We also set $\boldsymbol{u}_p = 0$ after 2005 for the latter two models in order to remove any transport effects from the solution. We normalize the ENA fluxes to their values in 2009 for easier comparison.

First, Figure 8 shows that large fluctuations anywhere between ∼10% and 50% over a timescale of 0.5–2 yr are primarily caused by the evolving neutral SW distribution. However, even without the time-dependent neutral SW, there is a gradual decrease in ENA fluxes from 2009 to 2015. This reduction is due to adiabatic cooling as the interstellar plasma density decreases during this time period. Thus, the decrease in ENA fluxes observed *IBEX* in 2012 is indeed due to a decrease in SW speed.

3.6. Effects of Interstellar Helium on the Ribbon Flux

An important assumption commonly made in current models of the heliosphere's interaction with the VLISM is the neglect of interstellar He plasma and neutral atoms and their dynamical effects on the heliosphere. Past studies have included the presence of interstellar He in the VLISM in an ad hoc manner. For example, Izmodenov et al. (2003) solved for the combined H and He plasma mixture and included their momentum and pressure but did not include the charge-exchange reactions between He and He^+. Müller & Zank (2004) studied the interaction of He/He^+ with H^+/H by charge exchange in the heliosphere but also ignored the charge-exchange interactions between He and He^+, which are much more important than the H^+/H and He/He^+ interactions. Kubiak et al. (2014) improved on earlier simulations by utilizing a 3D simulation of the heliosphere with a more realistic interstellar magnetic field draping outside the heliopause to investigate the secondary He population observed by *IBEX*. Later, Bzowski et al. (2017, 2019) utilized simulations of the heliosphere to directly calculate the *IBEX* He signal. However, these authors again did not include source terms for He + He^+ charge-exchange self-consistently, and thus their simulations of the heliosphere were not modified by the presence of He.

For the purposes of this study, we discuss the potential effects interstellar He^+ would have on our results. Approximately 40% of the dynamic pressure of the interstellar plasma is due to the presence of He^+ since their relative abundance compared to H is ∼10% (e.g., Slavin & Frisch 2008) and they have four times the mass of H. Since the charge-exchange cross section between He and He^+ is much larger than that between He and H^+ (or He^+ and H) at the energies of the VLISM plasma (e.g., Scherer et al. 2014), this implies that the inclusion of interstellar He in a simulation of the heliosphere would require a proportional decrease in proton density to keep the same dynamic pressure of the VLISM on the heliopause and maintain the distances of the TS and heliopause as observed by the *Voyager* spacecraft. By modeling the propagation of interstellar He through a simulated heliosphere, Bzowski et al. (2019) find that the interstellar He^+ density in the VLISM is approximately $9 \times 10^{-3}\,cm^{-3}$, or again, ∼10% of the expected H^+ abundance. Our heliosphere simulation in this study assumes a total effective plasma density of $0.09\,cm^{-3}$ in the VLISM, but in reality, the H^+ density should be ∼60% of this (or $0.054\,cm^{-3}$). With a smaller interstellar H^+ density, the filtration of neutral H through the heliosphere is reduced. Thus, in order to maintain a neutral H density of $\sim 0.1\,cm^{-3}$ at the frontward location of the TS location (Bzowski et al. 2009), the interstellar neutral H density must also be decreased. While the interaction between H^+ and neutral H is a nonlinear process and likely more complicated than what we describe, to zeroth order we estimate that neutral H must also decrease to 60% of its current simulated value.

Therefore, how do reduced interstellar H^+ and neutral H densities affect our results? First, this will decrease both the charge-exchange production (P) and loss (L) source terms by the same amount, resulting in a smaller total charge-exchange source term ($P - L$ is smaller). This implies that the effects of the evolving neutral SW distribution on the PUI distribution through charge exchange will be less significant. Second, the mean free path of neutralized SW outside the heliopause would increase by a factor of ∼1.7, which could potentially produce a ribbon source region that stretches farther from the heliopause into an ISMF that is less affected by the heliosphere (note that this will not "move" the PUI source region away from the heliopause, but rather stretch it out). Third, the production rate of ENAs is proportional to the interstellar neutral H density, and thus the ribbon ENA flux at 1 au is reduced.

While we currently cannot simulate the presence of interstellar He in the heliosphere–VLISM interaction in a self-consistent manner, we can simulate the effects of smaller interstellar H^+ and neutral H densities in our PINS/ENA model presented in this study by reducing the interstellar densities. In Figure 9 we show a comparison between the nominal model fluxes (shown in Figure 5) in ecliptic J2000 (278°, −9°) and a model where we reduce the interstellar H^+ and neutral H densities by 40%. When comparing the two model results normalized to their fluxes in 2009, it is clear that the inclusion of He, and thus reduction of H densities, yields an ENA flux that changes slightly less over time (see Figure 9, left panel). This is because the charge-exchange source term ($P - L$) is smaller, and thus any change in the PUI distribution from charge exchange is less effective. In the right panel of Figure 9 we show the absolute ENA intensities along with *IBEX* observations. We scale the *IBEX* data by a factor of 0.6 because they include ENAs from both the ribbon and GDF.

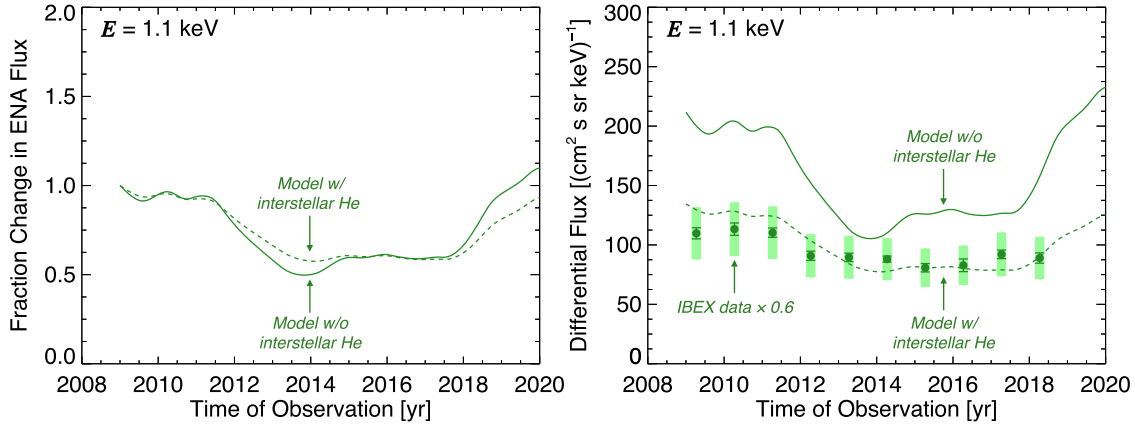

Figure 9. Simulated ENA fluxes at 1 au using the nominal model results from ecliptic J2000 (278°, −9°) and a model where we assume that the interstellar plasma and neutral densities are decreased by 40%. In the left panel we show the model fluxes normalized to their value in 2009. In the right panel we show the absolute fluxes alongside *IBEX* data, which are scaled by a factor of 0.6 to estimate the removal of GDF. *IBEX* 's statistical and systematic uncertainties are scaled accordingly.

While techniques to separate the ribbon from the GDF are not perfect, estimates of their relative intensities suggest that the GDF represents a significant fraction of the total intensity in the center of the ribbon at 1.1 keV (Schwadron et al. 2011, 2014). By approximating the relative contribution of the GDF (we assume that the GDF is 40% of the total flux) and subtracting its signal from *IBEX* data in Figure 9, our model compares well with the observations. This strongly supports the importance of including the effects of interstellar He models and analyses of ENA observations from the outer heliosphere.

4. Discussion and Conclusions

In this study we simulated the effects of the time-dependent SW derived from the OMNI database of observations at 1 au on the distribution of PUIs outside the heliopause and secondary ENA fluxes that form the *IBEX* ribbon. Here we discuss the implications of our results on the current state of the observations and offer predictions for the future.

4.1. Interstellar Shocks versus Evolving Neutralized SW Distribution

We have shown in Section 3 and Figures 2 and 8 that the evolution of the neutralized SW distribution and its conversion to PINS outside the heliopause by charge exchange are primarily responsible for the evolution of ribbon ENA fluxes at 1 au. Variations in the neutralized SW distribution are a direct result of the SW emission from the Sun. While merged interaction regions can propagate outside the heliopause and compress and heat PUIs in the VLISM, they only moderately affect the total PUI distribution at short intervals in time. In fact, as shown in Figure 3, there appear to be multiple shocks propagating through the PINS distribution outside the heliopause at any point in time. In this case, the resulting ENA flux at 1 au is, on average, not significantly changing over time. Rather, the injection of new PUIs outside the heliopause that can create ENAs observed by *IBEX* strongly depends on the neutralized SW distribution, and in particular changes in its bulk radial speed.

We note that our assumptions in modeling the neutral SW distribution may affect our results. In particular, we assumed that the neutral SW, whose properties we extract from a multifluid simulation, does not change in transverse temperature over time (i.e., transverse to the radial direction). Rather, since the average temperature of the neutral SW is expected to be much smaller than the radial spread in speed (e.g., Florinski & Heerikhuisen 2017), we assumed that the transverse temperature of the neutral SW is constant at 5000 K. In reality, the neutral SW temperature likely changes over time and can increase by a few factors. On the other hand, while SW conditions are intermittent at short timescales near 1 au, at larger distances from the Sun, where a significant number of neutral SW particles are created, structures in the SW have worn down via stream interactions. Nevertheless, while it is currently beyond our capability to properly model this effect, we expect that changes in the neutral SW temperature still could affect the PINS distribution outside the heliopause. For example, a larger neutral SW temperature would produce a broader angular ring beam of PINS, and thus a higher probability to produce secondary ENAs observable by *IBEX* at 1 au at angles farther from $\boldsymbol{B}\cdot\boldsymbol{r}=0$. This, in effect, would broaden the ribbon observed at 1 au but also reduce the ribbon flux near its peak. Interestingly, this then suggests that the width of the ribbon could change on timescales similar to the changing neutral SW distribution, possibly as a function of latitude and ENA energy.

4.2. Effects of Interstellar Helium and SW Alpha Particles

In Section 3.6 we showed that the inclusion of interstellar He in our model results can better reproduce *IBEX* observations. Currently, there are no models of the heliosphere that self-consistently include the dynamical effects of interstellar He on the SW–VLISM interaction, and it is likely important to include in order to reconcile multiple spacecraft observations.

We note that a potentially significant source of uncertainty in our calculations is the lack of SW alpha particles in our model. The addition of alpha particles in the simulation would provide an additional pressure on the heliopause and thus would require us to increase the interstellar plasma density a certain amount in order to maintain the same heliopause distance. *Wind* observations of the alpha-to-proton density in the SW show that it is typically between ∼1% and 5% near the ecliptic plane at 1 au (e.g., Alterman & Kasper 2019). The alpha-to-proton ratio changes as a function of latitude, with *Ulysses* observations showing a ratio of 4.4% in the fast SW and 2.3% in the slow SW (McComas et al. 2000; Ebert et al. 2009). *New Horizons*' SWAP observations of the SW at ∼20–40 au from the Sun show a similar ratio (Elliott et al. 2018). SWAP

observations show that the median of the alpha-to-proton density ratio is approximately 2.5% (see Figure 6 in Elliott et al. 2018). Taking this value, we estimate that the relative dynamic pressure of SW alphas to protons in the outer heliosphere is approximately 10%. Therefore, the additional pressure on the heliopause from alpha particles would require a corresponding increase in interstellar plasma pressure by ∼10% to maintain a heliopause distance consistent with *Voyager* observations (note, however, that the heliopause radial distance from the Sun changes over time, but we do not discuss it here). We do not know how much of this additional pressure is accounted for in interstellar protons, but if we assume that it is spread equally between the density of protons and He ions, then this suggests that the interstellar proton density is higher by ∼10%, and the results of our model with interstellar He in Figure 9 (dashed curve) should be scaled upward by ∼10%. The inclusion of SW alpha particles would slightly counteract the extra pressure on the heliosphere by interstellar He, although only by a small fraction. This also suggests that the estimated number density for interstellar He of $\sim 0.009\,\mathrm{cm}^{-3}$ is slightly overestimated if SW alpha particles are taken into account but is still within the uncertainties reported by Bzowski et al. (2019).

4.3. Predictions for Ribbon ENA Fluxes Observed after 2018

Our simulation predicts (see Figures 5, 7, and 9) that ribbon ENA fluxes at 1 au will begin to increase significantly after 2018, reaching a flux level similar to that observed early in the mission (before 2012) in 2019 and perhaps at higher levels in 2020. This predicted increase is primarily caused by an increase in SW speed emitted from the Sun (and thus neutralized SW in the outer heliosphere), increasing the production of 1.1 keV PUIs outside the heliopause. This increase in SW output was observed at 1 au in late 2014 and has already affected the GDF observed by *IBEX* starting in late 2016 (McComas et al. 2018, 2019). Future *IBEX* observations will test the accuracy of our model's prediction and provide a constraint on the source of the *IBEX* ribbon.

E.Z. acknowledges support from NASA grants 80NSSC17K0597 and 80NSSC18K1212. T.K. is supported by NASA grant 80NSSC19K0008, AFOSR award FA9550-19-1-0027, and STScI grant *HST*-GO-15380.002-A. P.M. acknowledges the support of NASA Earth and Space Science Fellowship Program grant 16-HELIO16F-0022 and the Johns Hopkins University Applied Physics Laboratory Independent Research and Development Funds. J.H. and N.P. were supported, in part, by NASA grants NNX16AG83G, 80NSSC18K1212, and 80NSSC18K1649. MS-FLUKSS simulations were supported by NSF grants OAC-1811176 and XSEDE MCA07S033 and NASA allocation HEC-SMD-17-1537. Supercomputer time allocations were provided on SGI Pleiades by NASA High End Computing Program award SMD 16 7570 and on TACC Stampede2 and SDSC Comet by NSF XSEDE project MCA07S033. The authors also acknowledge use of the SPDF COHOWeb database for OMNI data. E.Z. thanks Jamey Szalay for providing *IBEX* ENA data for the early part of 2018 (McComas et al. 2019). This work was also funded by the *IBEX* mission as part of the NASA Explorer Program (80NSSC18K0237).

Appendix
Solving the Parker Transport Equation

We follow the method of Zirnstein et al. (2018b) to solve Equation (1). First, to simplify the adiabatic heating term in Equation (1), it is written in natural logarithm in velocity space where $w = \ln(v)$:

$$\frac{\partial f}{\partial t} + u_\mathrm{p}\frac{\partial f}{\partial r} = \frac{1}{3}(\nabla\cdot\boldsymbol{u}_\mathrm{p})\frac{\partial f}{\partial w} + [f^* n_\mathrm{p} - f n_\mathrm{H}]\sigma_\mathrm{ex} v. \quad (12)$$

The PINS distribution f is solved over a range of speeds (∼200–700 $\mathrm{km\,s^{-1}}$) centered on the nominal ENA energy of *IBEX-Hi*'s energy passband 3 (1.1 keV, or 460 $\mathrm{km\,s^{-1}}$). The speed bin sizes range from ∼5 to 15 $\mathrm{km\,s^{-1}}$.

Because this study involves abrupt jumps in plasma density that can lead to the propagation of numerical uncertainties, we solve Equation (12) using an explicit, forward-time, upwind-difference scheme, where both the advection and adiabatic heating terms are solved with a first-order upwind scheme (e.g., Section 20.1.3, Press et al. 2007). While it is only first-order accurate, it prevents transport errors that may arise in the case for the second-order, central-difference scheme, which may propagate abrupt changes in plasma in both spatial directions, not just the advected direction. Equation (12) is rewritten as

$$f_{i,j}^{k} = f_{i,j}^{k-1} - u_{\mathrm{p},i}^{k-1}A_{i,j}^{k-1}\Delta t + \frac{1}{3}(\nabla\cdot\boldsymbol{u}_{\mathrm{p},i}^{k-1})B_{i,j}^{k-1}\Delta t + [f_{i,j}^{*\,k-1}n_{\mathrm{p},i}^{k-1} - f_{i,j}^{k-1}n_{\mathrm{H},i}^{k-1}]\sigma_\mathrm{ex}(v_j)v_j\Delta t, \quad (13)$$

where i, j, and k are grid indices for the space, velocity, and time coordinates, and $\Delta t = t_k - t_{k-1} =$ constant. The divergence term in Equation (3) and substituted into Equation (13) is solved with a second-order, central-difference method in space. As discussed above, the functions $A_{i,j}^{k-1}$ and $B_{i,j}^{k-1}$ are the upwind differences of the advection and adiabatic heating terms, respectively, given by

$$A_{i,j}^{k-1} = \begin{cases} \dfrac{f_{i,j}^{k-1} - f_{i-1,j}^{k-1}}{\Delta r}, & \text{if } u_{\mathrm{p},i}^{k-1} > 0 \\ \dfrac{f_{i+1,j}^{k-1} - f_{i,j}^{k-1}}{\Delta r}, & \text{if } u_{\mathrm{p},i}^{k-1} \leqslant 0 \end{cases}$$

$$B_{i,j}^{k-1} = \begin{cases} \dfrac{f_{i,j}^{k-1} - f_{i,j-1}^{k-1}}{\Delta w}, & \text{if } (\nabla\cdot\boldsymbol{u}_{\mathrm{p},i}^{k-1}) > 0 \\ \dfrac{f_{i,j+1}^{k-1} - f_{i,j}^{k-1}}{\Delta w}, & \text{if } (\nabla\cdot\boldsymbol{u}_{\mathrm{p},i}^{k-1}) \leqslant 0 \end{cases}, \quad (14)$$

where the velocity grid size Δw is independent of j and the spatial grid size Δr is independent of i. The grid sizes must satisfy the Courant–Friedrichs–Lewy stability conditions (e.g., Section 20.1.2, Press et al. 2007) driven by the advection and adiabatic heating terms, respectively given by

$$\frac{|u_{\mathrm{p,r}}|\,\Delta t}{\Delta r} \leqslant 1, \qquad \frac{|\nabla\cdot\boldsymbol{u}_\mathrm{p}|\,\Delta t}{3\Delta w} \leqslant 1. \quad (15)$$

ORCID iDs

E. J. Zirnstein https://orcid.org/0000-0001-7240-0618
T. K. Kim https://orcid.org/0000-0003-0764-9569
P. Mostafavi https://orcid.org/0000-0002-3808-3580
J. Heerikhuisen https://orcid.org/0000-0001-7867-3633
D. J. McComas https://orcid.org/0000-0001-6160-1158
N. V. Pogorelov https://orcid.org/0000-0002-6409-2392

References

Alterman, B. L., & Kasper, J. C. 2019, ApJL, 879, L6
Baranov, V. B., Lebedev, M. G., & Ruderman, M. S. 1979, Ap&SS, 66, 441
Borovikov, S. N., Pogorelov, N. V., Burlaga, L. F., & Richardson, J. D. 2011, ApJL, 728, L21
Burlaga, L. F., Ness, N. F., Gurnett, D. A., & Kurth, W. S. 2013, ApJL, 778, L3
Bzowski, M., Czechowski, A., Frisch, P. C., et al. 2019, ApJ, 882, 60
Bzowski, M., Kubiak, M. A., Czechowski, A., & Grygorczuk, J. 2017, ApJ, 845, 15
Bzowski, M., Möbius, E., Tarnopolski, S., Izmodenov, V., & Gloeckler, G. 2009, SSRv, 143, 177
Bzowski, M., Swaczyna, P., Kubiak, M. A., et al. 2015, ApJS, 220, 28
Chalov, S. V., Alexashov, D. B., McComas, D., et al. 2010, ApJL, 716, L99
Dayeh, M. A., Allegrini, F., DeMajistre, R., et al. 2014, ApJ, 797, 57
Dayeh, M. A., McComas, D. J., Livadiotis, G., et al. 2011, ApJ, 734, 29
Dayeh, M. A., Zirnstein, E. J., Desai, M. I., et al. 2019, ApJ, 879, 84
Desai, M. I., Allegrini, F., Bzowski, M., et al. 2014, ApJ, 780, 98
Desai, M. I., Dayeh, M. A., Allegrini, F., et al. 2019, ApJ, 875, 91
Ebert, R. W., McComas, D. J., Elliott, H. A., Forsyth, R. J., & Gosling, J. T. 2009, JGR, 114, A01109
Elliott, H. A., McComas, D. J., & DeForest, C. E. 2016, ApJ, 832, 66
Elliott, H. A., Valek, P., McComas, D. J., et al. 2018, ApJ, 866, 85
Florinski, V., & Heerikhuisen, J. 2017, ApJ, 838, 50
Florinski, V., Heerikhuisen, J., Niemiec, J., & Ernst, A. 2016, ApJ, 826, 197
Florinski, V., Zank, G. P., Heerikhuisen, J., Hu, Q., & Khazanov, I. 2010, ApJ, 719, 1097
Frisch, P. C., Heerikhuisen, J., Pogorelov, N. V., et al. 2010, ApJ, 719, 1984
Funsten, H. O., Allegrini, F., Bochsler, P., et al. 2009a, SSRv, 146, 75
Funsten, H. O., Allegrini, F., Crew, G. B., et al. 2009b, Sci, 326, 964
Funsten, H. O., DeMajistre, R., Frisch, P. C., et al. 2013, ApJ, 776, 30
Fuselier, S. A., Allegrini, F., Bzowski, M., et al. 2012, ApJ, 754, 14
Fuselier, S. A., Allegrini, F., Bzowski, M., et al. 2014, ApJ, 784, 89
Fuselier, S. A., Allegrini, F., Funsten, H. O., et al. 2009, Sci, 326, 962
Gamayunov, K., Zhang, M., & Rassoul, H. 2010, ApJ, 725, 2251
Gamayunov, K. V., Heerikhuisen, J., & Rassoul, H. 2017, ApJ, 845, 63
Gamayunov, K. V., Heerikhuisen, J., & Rassoul, H. K. 2019, ApJL, 876, L21
Gurnett, D. A., Kurth, W. S., Burlaga, L. F., & Ness, N. F. 2013, Sci, 341, 1489
Gurnett, D. A., Kurth, W. S., Stone, E. C., et al. 2015, ApJ, 809, 121
Heerikhuisen, J., Gamayunov, K. V., Zirnstein, E. J., & Pogorelov, N. V. 2016, ApJ, 831, 137
Heerikhuisen, J., & Pogorelov, N. V. 2011, ApJ, 738, 29
Heerikhuisen, J., Pogorelov, N. V., Zank, G. P., et al. 2010, ApJL, 708, L126
Isenberg, P. A. 2014, ApJ, 787, 76
Isenberg, P. A. 2015, JPCS, 577, 012014
Izmodenov, V., Malama, Y. G., Gloeckler, G., & Geiss, J. 2003, ApJL, 594, L59
Kim, T. K., Pogorelov, N. V., & Burlaga, L. F. 2017, ApJL, 843, L32
Kim, T. K., Pogorelov, N. V., Zank, G. P., Elliott, H. A., & McComas, D. J. 2016, ApJ, 832, 72
Kubiak, M. A., Bzowski, M., Sokół, J. M., et al. 2014, ApJS, 213, 29
Kubiak, M. A., Swaczyna, P., Bzowski, M., et al. 2016, ApJS, 223, 25
Leonard, T. W., Möbius, E., Bzowski, M., et al. 2015, ApJ, 804, 42
Lindsay, B. G., & Stebbings, R. F. 2005, JGR, 110, A12213
Liu, K., Möbius, E., Gary, S. P., & Winske, D. 2012, JGR, 117, A10102
Livadiotis, G., & McComas, D. J. 2011, ApJ, 741, 88
McComas, D. J., Allegrini, F., Bochsler, P., et al. 2009a, Sci, 326, 959
McComas, D. J., Allegrini, F., Bochsler, P., et al. 2009b, SSRv, 146, 11
McComas, D. J., Barraclough, B. L., Funsten, H. O., et al. 2000, JGR, 105, 10419
McComas, D. J., Bzowski, M., Fuselier, S. A., et al. 2015, ApJS, 220, 22
McComas, D. J., Dayeh, M. A., Allegrini, F., et al. 2012, ApJS, 203, 1
McComas, D. J., Dayeh, M. A., Funsten, H. O., et al. 2018, ApJL, 856, L10
McComas, D. J., Dayeh, M. A., Funsten, H. O., et al. 2019, ApJ, 872, 127
McComas, D. J., Lewis, W. S., & Schwadron, N. A. 2014, RvGeo, 52, 118
McComas, D. J., Zirnstein, E. J., Bzowski, M., et al. 2017, ApJS, 229, 41
Min, K., & Liu, K. 2018, ApJ, 852, 39
Möbius, E., Bochsler, P., Bzowski, M., et al. 2009, Sci, 326, 969
Möbius, E., Bzowski, M., Frisch, P. C., et al. 2015, ApJS, 220, 24
Möbius, E., Liu, K., Funsten, H., Gary, S. P., & Winske, D. 2013, ApJ, 766, 129
Mostafavi, P., & Zank, G. P. 2018a, ApJL, 854, L15
Mostafavi, P., & Zank, G. P. 2018b, JPCS, 1100, 012018
Mostafavi, P., Zank, G. P., Zirnstein, E. J., & McComas, D. J. 2019, ApJL, 878, L24
Müller, H.-R., & Zank, G. P. 2004, in AIP Conf. Proc. 719, Physics of the Outer Heliosphere, ed. V. Florinski, N. V. Pogorelov, & G. P. Zank (Melville, NY: AIP), 99
Niemiec, J., Florinski, V., Heerikhuisen, J., & Nishikawa, K.-I. 2016, ApJ, 826, 198
Osher, S. J., & Fedkiw, R. P. 2002, Level Set Methods and Dynamic Implicit Surfaces (New York: Springer)
Park, J., Kucharek, H., Möbius, E., et al. 2014, ApJ, 795, 97
Park, J., Kucharek, H., Möbius, E., et al. 2016, ApJ, 833, 130
Parker, E. N. 1961, ApJ, 134, 20
Parker, E. N. 1965, P&SS, 13, 9
Pogorelov, N., Borovikov, S., Heerikhuisen, J., et al. 2014, in Proc. 2014 Annual Conf. Extreme Science and Engineering Discovery Environment, ed. S. Lathrop & J. Alameda (New York: ACM), 22
Pogorelov, N. V., Heerikhuisen, J., Roytershteyn, V., et al. 2017, ApJ, 845, 9
Pogorelov, N. V., Heerikhuisen, J., Zank, G. P., et al. 2011, ApJ, 742, 104
Pogorelov, N. V., Zank, G. P., & Ogino, T. 2006, ApJ, 644, 1299
Press, W. H., Teukolsky, S. A., Vetterling, W. T., & Flannery, B. P. 2007, Numerical Recipes in C++: The Art of Scientific Computing (3rd ed.; Cambridge: Univ. Press Cambridge)
Rankin, J. S., Stone, E. C., Cummings, A. C., et al. 2019, ApJ, 873, 46
Reisenfeld, D. B., Bzowski, M., Funsten, H. O., et al. 2016, ApJ, 833, 277
Roytershteyn, V., Pogorelov, N. V., & Heerikhuisen, J. 2019, ApJ, 881, 65
Scherer, K., Fichtner, H., Fahr, H.-J., Bzowski, M., & Ferreira, S. E. S. 2014, A&A, 563, A69
Schwadron, N. A., Allegrini, F., Bzowski, M., et al. 2011, ApJ, 731, 56
Schwadron, N. A., Allegrini, F., Bzowski, M., et al. 2018, ApJS, 239, 1
Schwadron, N. A., Bzowski, M., Crew, G. B., et al. 2009, Sci, 326, 966
Schwadron, N. A., & McComas, D. J. 2013, ApJ, 764, 92
Schwadron, N. A., Möbius, E., Leonard, T., et al. 2015, ApJS, 220, 25
Schwadron, N. A., Möbius, E., McComas, D. J., et al. 2016, ApJ, 828, 81
Schwadron, N. A., Moebius, E., Fuselier, S. A., et al. 2014, ApJS, 215, 13
Sethian, J. A. 1999, Level Set Methods and Fast Marching Methods (Cambridge: Cambridge Univ. Press)
Slavin, J. D., & Frisch, P. C. 2008, A&A, 491, 53
Sokół, J. M., Kubiak, M. A., Bzowski, M., et al. 2015, ApJS, 220, 27
Summerlin, E. J., Viñas, A. F., Moore, T. E., Christian, E. R., & Cooper, J. F. 2014, ApJ, 793, 93
Swaczyna, P., Bzowski, M., Kubiak, M. A., et al. 2015, ApJS, 220, 26
Swaczyna, P., McComas, D. J., & Schwadron, N. A. 2019, ApJ, 871, 254
Zank, G. P. 1999, SSRv, 89, 413
Zank, G. P. 2015, ARA&A, 53, 449
Zank, G. P., Pauls, H. L., Williams, L. L., & Hall, D. T. 1996, JGR, 101, 21639
Zirnstein, E. J., Dayeh, M. A., McComas, D. J., & Sokół, J. M. 2017, ApJ, 846, 63
Zirnstein, E. J., Funsten, H. O., Heerikhuisen, J., et al. 2016a, ApJ, 826, 58
Zirnstein, E. J., Heerikhuisen, J., & Dayeh, M. A. 2018a, ApJ, 855, 30
Zirnstein, E. J., Heerikhuisen, J., Funsten, H. O., et al. 2016b, ApJL, 818, L18
Zirnstein, E. J., Heerikhuisen, J., & McComas, D. J. 2015a, ApJL, 804 L22
Zirnstein, E. J., Heerikhuisen, J., Pogorelov, N. V., McComas, D. J., & Dayeh, M. A. 2015b, ApJ, 804, 5
Zirnstein, E. J., Heerikhuisen, J., Zank, G. P., et al. 2014, ApJ, 783, 129
Zirnstein, E. J., Kumar, R., Heerikhuisen, J., McComas, D. J., & Galli, A. 2018b, ApJ, 860, 170
Zirnstein, E. J., McComas, D. J., Schwadron, N. A., et al. 2019a, ApJ, 876, 92
Zirnstein, E. J., Swaczyna, P., McComas, D. J., & Heerikhuisen, J. 2019b, ApJ, 879, 106